

Study of the Crystal Architecture, Optoelectronic Characteristics, and Nonlinear Optical Properties of 4-Amino Antipyrine Schiff Bases

Amsaveni Arumugam, Ramesh Shanmugam, Saravanabhavan Munusamy,* Shabbir Muhammad, Hamed Algarni, and Marimuthu Sekar*



Cite This: *ACS Omega* 2023, 8, 15168–15180



Read Online

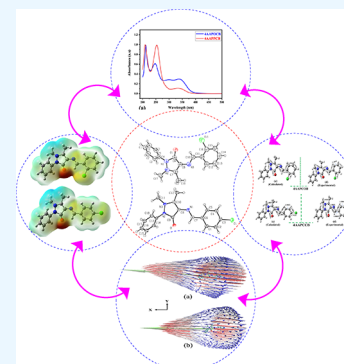
ACCESS |

Metrics & More

Article Recommendations

Supporting Information

ABSTRACT: Two Schiff bases, (*E*)-4-((2-chlorobenzylidene)amino)-1,5-dimethyl-2-phenyl-1,2-dihydro-3*H*-pyrazol-3-one (4AAPOCB) and (*E*)-4-((4-chlorobenzylidene)amino)-1,5-dimethyl-2-phenyl-1,2-dihydro-3*H*-pyrazol-3-one (4AAPCB), have been synthesized and grown as single crystals. Single-crystal X-ray diffraction analysis was employed to determine the crystal structure of the compounds, and the results suggest that the compounds crystallized into an orthorhombic crystal system having $P2_12_12_1$ and $Pbca$ space groups, respectively. Further, the crystallinity of the compounds was analyzed by the PXRD technique. The UV–vis–NIR spectra of the compounds demonstrate excellent transmittance in the entire visible region. The lower cutoff wavelengths of the compounds were determined to be 338 and 333 nm, respectively; additionally, optical band gaps of the compounds found were 4.60 and 4.35 eV. FTIR and NMR (^1H and ^{13}C) spectral techniques were utilized to analyze the molecular structure of the compounds. The compounds emit photoluminescence with broad emission bands with centers at 401 and 418 nm. The thermal stability and phase transitions were assessed through thermogravimetric methods. The phase transition prior to melting was indicated by the endothermic event at around 190 °C in the DTA curves of both crystals, and the same was observed in the DSC curves. The second harmonic efficiencies of the powdered compounds I and II were found to be 3.52 and 1.13 times better than that of the standard reference KDP. The 4AAPOCB and 4AAPCB compounds showed isotropic polarizability amplitudes of 46.02×10^{-24} and 46.52×10^{-24} esu, respectively. The calculation of linear polarizability and NLO second-order polarizability (β) along with other optical parameters was performed for optimized geometries. The nonzero amplitudes of the average β values for compounds 4AAPOCB and 4AAPCB were found to be 14.74×10^{-30} and 8.10×10^{-30} esu, respectively, which show a decent potential of the synthesized molecules for NLO applications. The calculated β amplitudes were further explained based on calculated electronic parameters like molecular electrostatic potentials, frontier molecular orbitals, molecular orbital energies, transition energies, oscillator strengths, and unit spherical representation of NLO polarizability. The current analysis emphasizes the significance of synthesized compounds as prospective candidates for optical and NLO applications through the use of experiments and quantum computations.



1. INTRODUCTION

Nonlinear optical materials are important in the modern era for a wide range of applications in photonics and optoelectronics.¹ Nonlinear optical materials play an important role in modern photonics and optoelectronics, and their use in a wide range of applications is likely to continue to grow in the future.² Organic nonlinear optical (NLO) materials are a class of materials that have gained significant attention in recent years due to their potential for use in a wide range of applications, including optical communications, data storage, and imaging.³ Organic NLO materials are typically based on organic molecules or polymers, and they exhibit nonlinear optical properties due to their high optical nonlinearity and large hyperpolarizability. One of the advantages of organic NLO materials is their ability to be synthesized and designed with specific properties, such as high thermal stability, high optical clarity, and tunable nonlinear optical properties.⁴ This allows for the development of materials with tailored

properties that can be optimized for specific applications. Among all the organic NLO materials, Schiff base materials represent a promising class of organic materials with unique properties and potential applications in a wide range of fields.⁵ Their molecular design and synthesis can be tailored to meet specific application requirements, making them a promising class of NLO materials.^{6,7}

Hugo Schiff first described Schiff bases, which are organic compounds produced when primary amines are condensed with aldehydes or ketones.⁸ They are called imines or azomethines, and they have gained the attention of researchers

Received: January 10, 2023

Accepted: April 3, 2023

Published: April 17, 2023



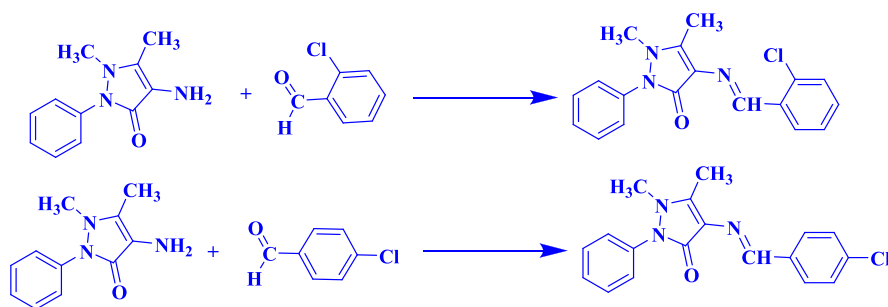


Figure 1. Reaction scheme for 4AAPOCB and 4AAPPCB.

due to their ease in synthesis and complex forming ability with almost all metals.⁹ Schiff bases are widely used in various fields like dyes and pigments, catalysis,¹⁰ optical chemical sensors,¹¹ cell imaging,¹² solar energy applications,¹⁰ corrosion inhibition,¹³ LED applications,¹⁴ renewable energy materials,¹⁵ and so on. The basic concept of Schiff base chemistry is profusely utilized to synthesize modern materials like COFs¹⁶ and MOFs,¹⁷ and it provides key aspects to enhance physicochemical properties and also sensing abilities. Schiff bases served as ligands and formed stable coordination complexes with metals; they proved to have a multifold increase of properties and activities leading to applications in various fields. Schiff bases recently received significant scientific interest in nonlinear optical (NLO) applications due to their enhanced intramolecular charge transfer properties, which usually lead to a better NLO response.^{18–20} Many types of organic compounds were reported to have different NLO responses in relation to their structural and NLO property aspects.^{21–24}

Schiff bases possess delocalized π -electron systems, synthetic flexibility, and high second-order nonlinear susceptibilities (χ^2), making this a fertile area of research.²⁵ Designing supramolecular organic network material with a π -conjugated backbone structure utilizing a molecular engineering approach with donor (D)–acceptor (A) functional groups between the molecules produces push–pull effects, comprising significant SHG and THG efficiency.^{26,27} Basic requirements for SHG efficiency are a lack of symmetry centers in molecules and significant change in dipole moment; the existence of donor–acceptor groups in conjugated systems enhances the SHG efficiency of the material. The SHG efficiency of a series of salicylaldehyde-based Schiff bases was investigated by Bhat *et al.* early in the literature.⁷ Organic NLO materials generally contain donor (D)–acceptor (A) groups linked through a π -electronic bridge enhancing molecular polarizability and getting good nonlinear response.¹⁴ Schiff bases and their complexes have also gained great attention as nonlinear materials due to their extensive π -conjugation and synthetic flexibility.^{28–31}

Among the organic classes, the 4-amino antipyrine (4AAP) is an excellent heterocyclic molecule capable of forming Schiff-base-type ligands used to synthesize a variety of chelating metal complexes. The astounding ability to form metal chelates paves the way to a great many applications in various fields.³² The Schiff base derivatives of 4AAP show significant pharmacological activities,³³ and recently, the sulfate salt of 4AAP, a charge transfer crystal, was synthesized, and its biological activities were analyzed.³⁴ In this paper, we are going to report the synthesis, crystal structure, spectroscopic analysis, and nonlinear efficiency of two Schiff-base-type crystals, namely, 4AAPOCB (I) and 4AAPPCB (II). Moreover, quantum

chemical methods are used to get more insight into their geometry and molecular nonlinearity.

The density functional theory (DFT) is a computational method used in condensed matter physics, materials science, and chemistry to study the electronic structure of molecules.³⁵ DFT calculations can provide insights into the electronic structure of molecules, materials, and surfaces. By calculating the electron density and other properties of the system, DFT can help researchers understand the chemical properties of a material, such as its reactivity, stability, catalytic activity, electronic properties, and so forth. DFT calculations of NLO properties have been used to design and optimize materials for NLO applications, such as frequency conversion and optical switching. DFT can be used to understand the mechanisms that give rise to nonlinear optical properties in materials.³⁶ By calculating the electronic structure of a molecule, it is possible to determine how the electron distribution changes in response to an applied electric field, which is key to understanding the nonlinear optical response.^{37–39}

2. EXPERIMENTAL METHODS

2.1. Synthesis and Microanalysis of the Schiff Base Compounds. Sigma Aldrich provided all of the synthesis starting materials, which were utilized as received. Schiff base compound I, (*E*)-4-((2-chlorobenzylidene)amino)-1,5-dimethyl-2-phenyl-1,2-dihydro-3*H*-pyrazol-3-one (4AAPOCB), was synthesized by reacting 4-aminoantipyrine (2.0324 g, 1 mmol) with 2-chlorobenzaldehyde (1.4057 g, 1 mmol). The starting compounds were dissolved in 20 mL of methanol separately and stirred by using a magnetic stirrer for 30 min to get a homogeneous solution. Drop by drop, the aldehyde solution was added to the amine; as a result, a light yellow precipitate gradually formed. The mixture was heated over a magnetic stirrer with constant stirring for 2 h, and then the precipitate was filtered through a Whatman 41-grade filter paper. The resulting precipitate was dried at room temperature. Its solubility was analyzed with various solvents, and the formation of the product was confirmed by thin layer chromatography. The same procedure was repeated to synthesize compound II ((*E*)-4-((4-chlorobenzylidene)amino)-1,5-dimethyl-2-phenyl-1,2-dihydro-3*H*-pyrazol-3-one (4AAPPCB)). The reaction scheme for the synthesis of Schiff base compounds is shown in Figure 1.

2.2. Solubility and Crystal Growth. The solubility of the compound is the key factor to determine the crystal growth. Neither good solubility nor poor solubility helps crystal growth; moderate solubility of the substance in a particular solvent is required.⁴⁰ Supersaturation and temperature are the driving forces in controlling the geometry, quality, and stability of the crystals. Solubility curves are helpful in choosing a

growth solvent and a method for crystallization. The temperature-dependent solubility of Schiff bases was determined using the polythermal method,⁴¹ and the resulting solubility curves are shown in Figure 2. The compounds that

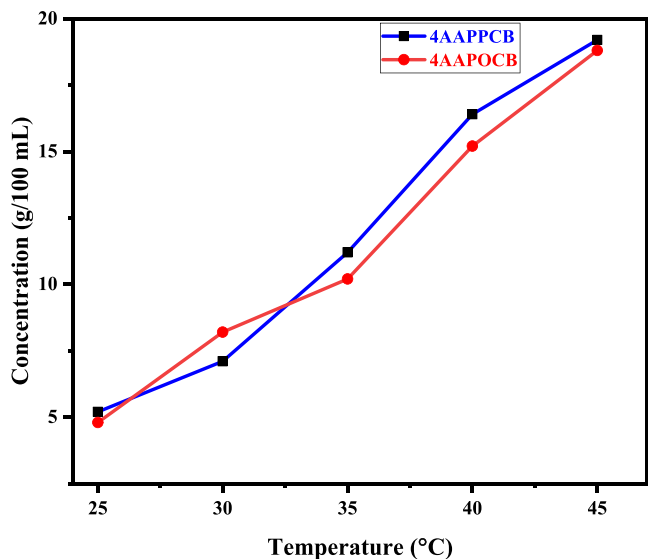


Figure 2. Solubility curves for 4AAPCB and 4AAPOCB in methanol.

were made are very soluble in solvents like acetonitrile, chloroform, DMSO, and DMF, and they are only moderately soluble in methanol and ethanol. A sufficient quantity of compounds I and II was dissolved in the solvent methanol using a temperature-controlled magnetic stirrer, and the mixture was thoroughly stirred to produce homogeneous solutions.

After 2 h of continuous stirring, the homogeneous solutions were filtered to remove suspended impurities using a Whatman 41-grade filter paper. After 15 days, the rod-shaped, pale yellow crystals were harvested from the beaker, which was tightly covered with aluminum foil with a few punched holes and kept in a dust-free environment for crystal growth.

2.3. Characterization Studies. Single-crystal X-ray diffraction analysis was used to determine both compounds' crystal structures. A Bruker Smart Apex CCD diffractometer equipped with Mo K α radiation of wavelength 0.71073 Å was used to collect reflection data using γ and ω scan methods. The structure of the crystals was solved by direct methods,⁴² and structure refinements were carried out by the full-matrix least squares technique employing SHELXS97⁴³ and refined by the full-matrix least squares procedure on F^2 . The purity and crystallinity of the samples were examined by powder X-ray diffraction using a Shimadzu LabX XRD-6100 X-ray diffractometer. To verify the quantity of various elements present in the crystal, elemental analysis was carried out employing an Elementar Vario EL III analyzer. The existence of different functional groups was examined by the FTIR spectrum recorded in the frequency range 4000 to 500 cm^{-1} using a Shimadzu FTIR Spirit spectrometer. In a methanol medium, the compounds' electronic spectra were observed and recorded using a Systronics double beam UV–visible spectrophotometer, and the UV–vis–NIR transmittance spectra of both the compounds were measured by employing a JASCO V-650 spectrophotometer. A Jobin Yvon Fluorolog

FL3-11 spectrofluorometer was used to analyze the crystals' emission characteristics at room temperature. The thermal analysis of the powder sample was performed between 30 and 750 °C by using a Mettler Toledo simultaneous thermal analyzer system at STIC Kochi. The SHG efficiency of the powdered sample was examined by using the Kurtz–Perry technique at the P.K. Das lab, IISc Bangalore.

2.3.1. Computational Methods. The Gaussian 16 software code was used for all quantum computations.⁴⁴ The molecules were optimized to their lowest ground states using DFT methods. The optimization was performed with the M06-2X functional and 6-31G* basis sets.⁴⁵ The optimized geometries were further explored by quantum chemical methods for their potential optical and NLO properties. The UV–visible spectra were computed using the time-dependent (TD) DFT method. For the calculation of linear polarizability and first hyperpolarizability, we used the polar keyword as implemented in Gaussian 16. The linear polarizability and first hyperpolarizability can be obtained through the following relationship given below, although more details can be found in our previous work.^{46–48}

The average isotropic polarizability (α_{iso}) can be calculated by the following equation:

$$\langle \alpha_{\text{iso}} \rangle = \frac{1}{3}(\alpha_{xx} + \alpha_{yy} + \alpha_{zz}) \quad (1)$$

For anisotropy of polarizability ($\Delta\alpha$) and average static second hyperpolarizability, these can be calculated by the following equation:

$$\Delta\alpha = \frac{1}{\sqrt{2}} \sqrt{[(\alpha_{xx} - \alpha_{yy})^2 + (\alpha_{yy} - \alpha_{zz})^2 + (\alpha_{zz} - \alpha_{xx})^2 + 6\alpha_{xz}^2]} \quad (2)$$

Meanwhile, first hyperpolarizability can be calculated as follows:

$$\beta_{//} = [(\beta_{xxx} + \beta_{xyy} + \beta_{zzz})^2 + (\beta_{yyy} + \beta_{yzz} + \beta_{yxx})^2 + (\beta_{zzz} + \beta_{zxx} + \beta_{zyy})^2]^{1/2} \quad (3)$$

Here, $\beta_{//}$ is the projection of the hyperpolarizability vector over the dipole moment.

3. RESULTS AND DISCUSSION

3.1. Elemental Analysis. The stoichiometric proportion and purity of the synthesized compounds were analyzed by CHNSO analysis. The elemental composition of chlorine atoms was calculated by subtracting the total composition of other atoms, and it was compared with the theoretical composition. The results obtained from the microanalysis showed that compound I (4AAPOCB) contains C: 66.24% (66.36%), H: 4.92% (4.95%), N: 12.88% (12.90%), O: 5.01% (4.91%), and Cl: 10.95% (10.88%). Compound II (4AAPCB) contains C: 66.33% (66.36%), H: 4.91% (4.95%), N: 12.84% (12.90%), O: 4.94% (4.91%), and Cl: 10.98% (10.88%). The elemental analysis data reveal that the experimentally determined values are in good agreement with theoretical values (within the bracket). The elemental analysis data are presented in Table 1.

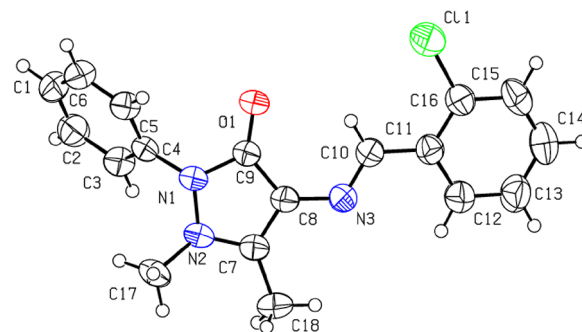
3.2. X-ray Crystal Structural Analysis. In addition to revealing the structural parameters of the single crystals, the X-

Table 1. Elemental Analysis Results of 4AAPOCB and 4AAPPCB

elements	calculated (%)	experimental (%)	
		4AAPOCB	4AAPPCB
carbon	66.36	66.24	66.33
hydrogen	4.95	4.92	4.91
nitrogen	12.90	12.88	12.84
oxygen	4.91	5.01	4.94
chlorine	10.88	10.95	10.98

ray diffraction results also reveal the nature of the space group. The crystal's optical properties are heavily influenced by its symmetry; the crystal must have non-centrosymmetric space groups to be SHG-active. By recrystallizing compounds I and II, high-quality single crystals with dimensions of $0.3 \times 0.35 \times 0.4$ and $0.41 \times 0.3 \times 0.17$ mm were used for X-ray diffraction analysis to ascertain the crystal structure and lattice parameters. 4AAPPCB's crystal belongs to the orthorhombic centrosymmetric *Pbca* space group, whereas 4AAPOCB's single crystal X-ray diffraction result shows that the compound crystallized into an orthorhombic crystal system with a non-centrosymmetric *P2₁2₁2₁* space group. Table 2 contains a list of the crystal data and structure refinement parameters derived from SCXRD analysis. The chlorine atom is attached to the para position of the phenyl ring in compound II, whereas the chlorine atom is attached to the ortho position of the phenyl ring in compound I. Because of the different positions of chlorine, isomers have

distinct space group structures. The ORTEP diagram of the asymmetric units of crystals I and II, which was drawn with an atom numbering scheme and a probability level of 50% thermal displacement ellipsoidal, is depicted in Figures 3 and 4. A single, isolated molecule is contained in each of the asymmetric units. Various bond lengths of compounds I and II are listed in Tables 3 and 4, respectively.

**Figure 3.** ORTEP diagram with the atom numbering scheme and optimized geometry of 4AAPOCB.

3.3. Powder X-ray Diffraction Analysis. The powder X-ray diffractograms of the samples were determined for compounds I and II and are presented in Figure 5. Powder X-ray patterns of both compounds showing sharp peaks indicated the crystallinity and purity of the samples.

Table 2. Crystal Data and Structure Refinement Parameters for 4AAPOCB and 4AAPPCB

identification code	4AAPOCB	4AAPPCB
empirical formula	C ₁₈ H ₁₆ ClN ₃ O	C ₁₈ H ₁₆ ClN ₃ O
formula weight	325.79	325.79
temperature	296 K	150(2) K
wavelength	0.71073 Å	0.71073 Å
crystal system	orthorhombic	orthorhombic
space group	<i>P2₁2₁2₁</i>	<i>Pbca</i>
unit cell dimensions	<i>a</i> = 6.8330(3) Å <i>b</i> = 13.6031(8) Å <i>c</i> = 17.5148(10) Å $\alpha = \beta = \gamma = 90^\circ$	<i>a</i> = 6.9878(4) Å <i>b</i> = 17.2746(1) Å <i>c</i> = 26.6878(19) Å $\alpha = \beta = \gamma = 90^\circ$
volume	1628.00(15) Å ³	3221.5(4) Å ³
Z	8	8
density (calculated)	1.329 g/cm ³	1.343 g/cm ³
absorption coefficient	0.242 mm ⁻¹	0.245 mm ⁻¹
F(000)	680	1360
crystal size	0.300 × 0.350 × 0.400 mm ³	0.410 × 0.300 × 0.170 mm ³
theta range for data collection	2.216 to 28.290°	2.809 to 27.915°
index ranges	-9 ≤ <i>h</i> ≤ 9, -18 ≤ <i>k</i> ≤ 18, -23 ≤ <i>l</i> ≤ 23	-9 ≤ <i>h</i> ≤ 9, -22 ≤ <i>k</i> ≤ 22, -35 ≤ <i>l</i> ≤ 35
reflections collected	28,592	57,971
independent reflections	3985 [<i>R</i> (int) = 0.0292]	3822 [<i>R</i> (int) = 0.0469]
completeness to theta = 25.242°, 28.90°	99%	98.8%
absorption correction	semi-empirical from equivalents	semi-empirical from equivalents
refinement method	full-matrix least squares on <i>F</i> ²	full-matrix least squares on <i>F</i> ²
data/restraints/parameters	3985/0/210	3822/0/208
goodness-of-fit on <i>F</i> ²	1.061	1.055
final <i>R</i> indices [<i>I</i> > 2σ(<i>I</i>)]	<i>R</i> 1 = 0.0432, w <i>R</i> 2 = 0.1353	<i>R</i> 1 = 0.0411, w <i>R</i> 2 = 0.1083
<i>R</i> indices (all data)	<i>R</i> 1 = 0.0485, w <i>R</i> 2 = 0.1403	<i>R</i> 1 = 0.0459, w <i>R</i> 2 = 0.1140
extinction coefficient	n/a	n/a
largest diff. peak and hole	0.40 and -0.32 e.Å ⁻³	0.348 and -0.274 e.Å ⁻³
CCDC no.	2248220	2225635

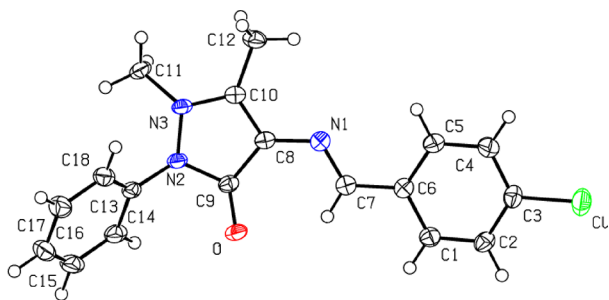


Figure 4. ORTEP diagram with the atom numbering scheme and optimized geometry of 4AAPPCB.

Table 3. Bond Lengths [Å] for the 4AAPOCB Crystal

atom A–atom B	bond lengths (Å)	atom A–atom B	bond lengths (Å)
Cl(1)–C(15)	1.7324(1)	C(11)–C(15)	1.3846(1)
O(1)–C(9)	1.2290(2)	C(11)–C(12)	1.3956
C(8)–N(3)	1.3860	C(16)–C(14)	1.3869(1)
C(8)–C(9)	1.4304	C(15)–H(14)	0.9300(1)
C(8)–C(7)	1.3699	C(15)–C(13)	1.3513
N(3)–C(10)	1.2789	C(14)–H(13)	0.9300(1)
N(2)–N(1)	1.3969(1)	C(14)–C(10)	1.3711
N(2)–C(16)	1.4502(1)	C(6)–H(6)	0.9300(1)
N(2)–C(7)	1.3504(1)	C(6)–C(5)	1.3729
C(1)–H(1)	0.9300(1)	C(5)–H(5)	0.9300(1)
C(1)–C(2)	1.3754	C(17)–H(17A)	0.9600(1)
C(1)–C(6)	1.3646	C(17)–H(17B)	0.9600(1)
C(2)–H(2)	0.9300(1)	C(17)–H(17C)	0.9600(1)
C(2)–C(3)	1.3787	C(7)–C(17)	1.4727(1)
C(30)–H(3)	0.9300(1)	C(13)–H(10)	0.9300(1)
C(3)–C(4)	1.3779	C(10)–C(12)	1.3679
C(4)–N(1)	1.4142	C(12)–H(12)	0.9300(1)
C(4)–C(5)	1.3772	C(18)–H(18A)	0.9600(1)
N(1)–C(9)	1.4000	C(18)–H(18B)	0.9600(1)
C(10)–H(10)	0.9300(1)	C(18)–H(18C)	0.9600(1)
C(10)–C(11)	1.4558		

Table 4. Bond Lengths [Å] for the 4AAPPCB Crystal

atom A–atom B	bond lengths (Å)	atom A–atom B	bond lengths (Å)
Cl–C(3)	1.7418(14)	C(8)–C(10)	1.3746(17)
O–C(9)	1.2338(15)	C(8)–C(9)	1.4405(18)
N(1)–C(7)	1.2836(17)	C(10)–C(12)	1.4822(18)
N(1)–C(8)	1.3896(17)	C(11)–H(11A)	0.9800
N(2)–C(9)	1.4097(17)	C(11)–H(11B)	0.9800
N(2)–N(3)	1.4066(14)	C(11)–H(11C)	0.9800
N(2)–C(10)	1.4217(18)	C(12)–H(12A)	0.9800
N(3)–C(10)	1.3589(17)	C(12)–H(12B)	0.9800
N(3)–C(11)	1.4635(17)	C(12)–H(12C)	0.9800
C(1)–C(2)	1.386(2)	C(13)–C(17)	1.390(2)
C(1)–C(6)	1.3941(19)	C(13)–C(13)	1.3926(19)
C(1)–H(1B)	0.9500	C(14)–C(14)	1.390(2)
C(2)–C(3)	1.382(2)	C(14)–H(14A)	0.9500
C(2)–H(2A)	0.9500	C(15)–C(15)	1.383(3)
C(3)–C(4)	1.387(2)	C(15)–H(15A)	0.9500
C(4)–C(5)	1.384(2)	C(16)–C(16)	1.385(2)
C(4)–H(4A)	0.9500	C(16)–H(16A)	0.9500
C(5)–C(6)	1.399(2)	C(17)–C(17)	1.388(2)
C(5)–H(5A)	0.9500	C(17)–H(17A)	0.9500
C(6)–C(7)	1.4665(19)	C(18)–H(18A)	0.9500
C(7)–H(7A)	0.9500		

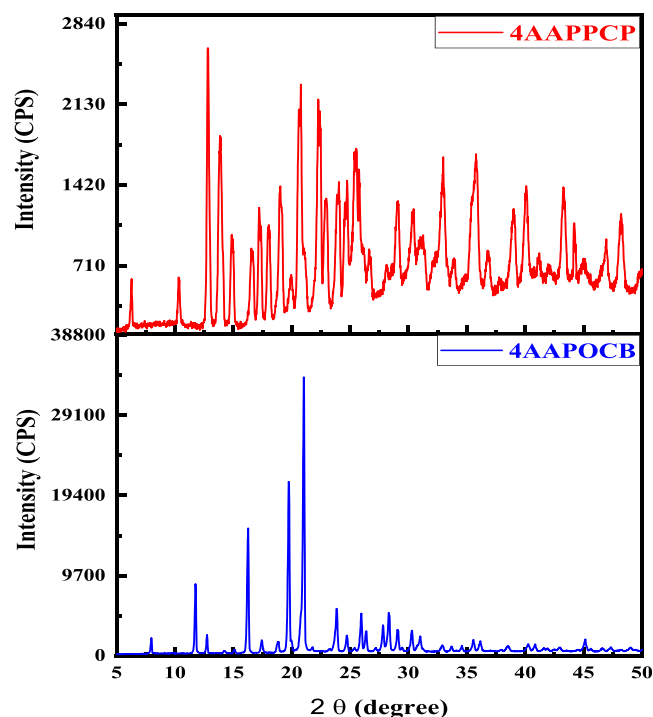


Figure 5. PXRD patterns of compounds 4AAPPCB and 4AAPOCB.

3.4. Electronic Spectral Analysis. The optical properties of organic molecules can be thoroughly examined using UV–vis–NIR spectroscopy. In Figure 6, three absorption bands are depicted in the UV–visible spectrum of compounds I and II recorded in a methanol medium. Evidently, the presence of methanol is the cause of the first absorption bands at 209 and 211 nm; the lower cutoff for methanol is 210 nm.⁴⁹ The second absorption bands for compounds I and II observed at (λ_{\max}) 247 and 254 nm are attributed to symmetry forbidden π – π^* transitions of the aromatic ring; usually, the existence of reactive functional groups in the aromatic ring causes a red shift. The second bands for compounds I and II noted at λ_{\max} 338 and 333 nm are due to n – π^* transitions of C=N and C=O groups.⁵⁰ The n – π^* transitions of the carbonyl group are usually observed at 310–330 nm and these excitations may be coupled with n – π^* transitions of the C=N bond, then it may shift to a slightly higher wavelength. Besides this, we have also calculated the UV–visible spectra of 4AAPCOB and 4AAPPCB using quantum computational methods with the M06-2X functional and 6-31G* basis set as given in Figure 6. There is a reasonable agreement among experimental and calculated UV–visible spectra of 4AAPCOB and 4AAPPCB. The first absorption peaks in calculated spectra are around 230 to 240 nm, which are closer to their counterpart experimental peaks at 247 and 254 nm. In contrast, the second absorption peaks in the computed spectra range from 275 to 325 nm, which are close to the experimental peaks of 338 and 333 nm. The frontier molecular orbitals in the proceeding section indicate their mixed nature like π – π^* and n – π^* transitions as explained in the above experimental section.

3.4.1. Determination of Optical Parameters. We can work out the optical band gap of the material by involving UV light retention as a beginning stage for the electron excitation from the valence band to the conduction band. The following relation is used to convert absorption wavelength into excitation energy:

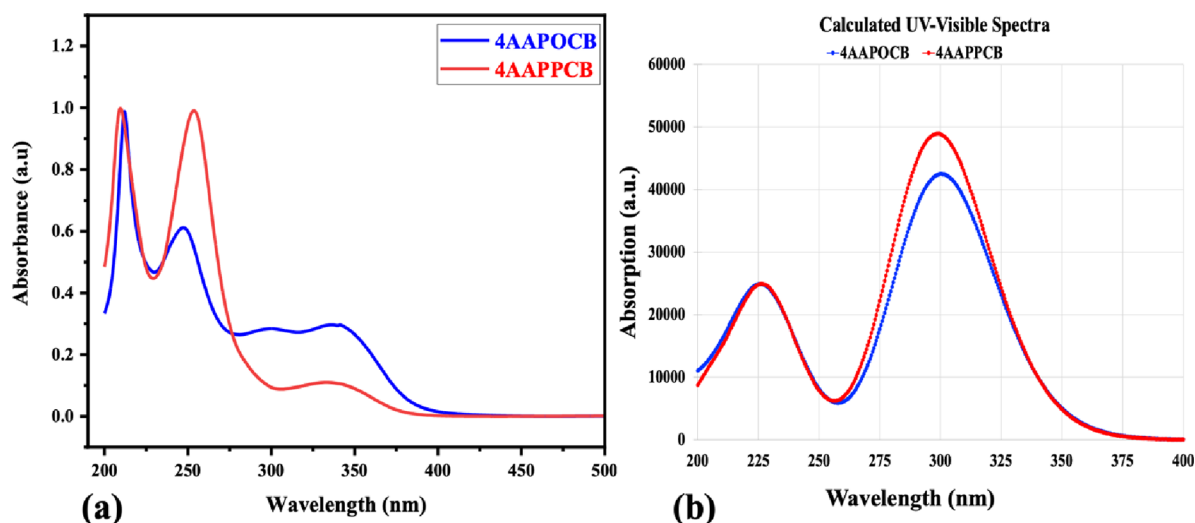


Figure 6. The experimental (a) and calculated (b) UV–visible absorption spectra of the compounds 4AAPOCB and 4AAPCCB at the TD-M06-2X/6-31G* method.

$$E_g = \frac{hc}{\lambda_{\max(\text{nm})}} \quad (\text{or}) \quad E_g = \frac{1240}{\lambda} \text{ eV} \quad (4)$$

where c is the speed of light, h is Planck's constant, and λ is the sample's cutoff wavelength. Compounds I and II had calculated band gaps (E_g 's) of 3.66 and 3.72 eV, respectively. The crystal's absorption coefficient (α) can be calculated using the following equation:

$$\alpha = \frac{2.303 \log(1/T)}{t} \quad (5)$$

where T is transmittance and t is the thickness of the crystal used. The direct optical gap of the grown crystal can be calculated by exploiting the dependence photon energy ($h\nu$) upon the absorption coefficient (α) according to the following equation:

$$(\alpha h\nu)^2 = A(h\nu - E_g) \quad (6)$$

Figures 7 and 8 depict Tauc's plot and the UV–vis–NIR transmittance spectra of compounds I and II. The lower cut wavelengths of Schiff base compounds I and II are 338 and 333 nm, respectively, indicating that there is no significant absorption in the entire visible and NIR regions as determined by the transmittance spectra of the compounds. Extrapolating a straight line from the absorption edge to the x axis, $(\alpha h\nu)^2 = 0$ (Tauc's plot) yielded an estimate of the band gap energy. The crystals were found to have an optical band gap of 4.60 and 4.35 eV. The crystals' wide band gap and good optical transparency suggest that they could be used in optical applications.

3.5. Photoluminescence Studies. The photoluminescence emission spectra of the Schiff bases I and II were carried out in methanol at room temperature. The emission spectra of the compounds I and II are presented in Figure 9, and broad emission bands appeared at 418 nm (2.96 eV) and 401 nm (3.09 eV) indicating the presence of violet emission. The broad emission band in the violet region is attributed to π – π^* intraligand transitions, and the conjugated π -electronic structure of the Schiff bases causes broad emission bands.

3.6. Fourier Transformed Infrared (FTIR) Spectral Analysis. The FTIR spectra of compounds 4AAPOCB and

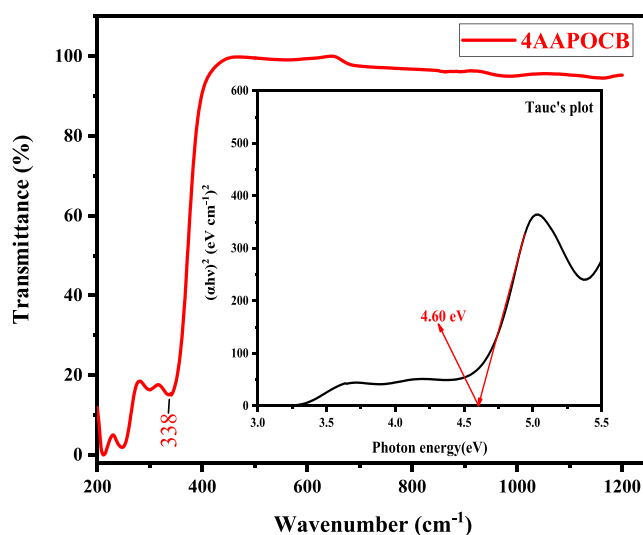


Figure 7. UV–vis–NIR transmittance spectrum of 4AAPOCB (inset: Tauc's plot).

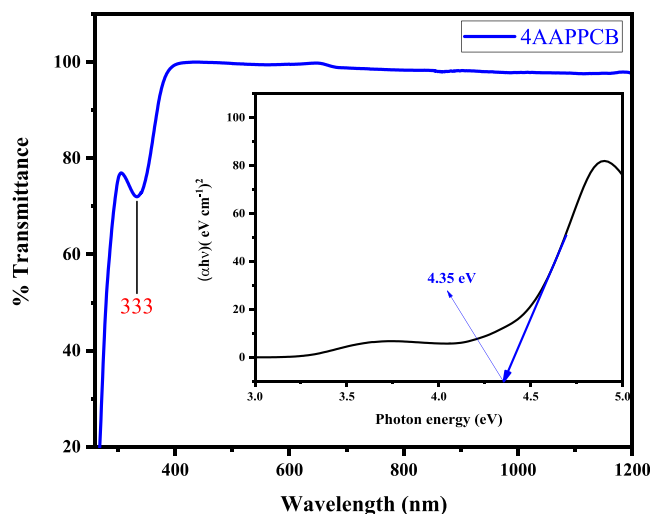


Figure 8. UV–vis–NIR transmittance spectrum of 4AAPCCB (inset: Tauc's plot).

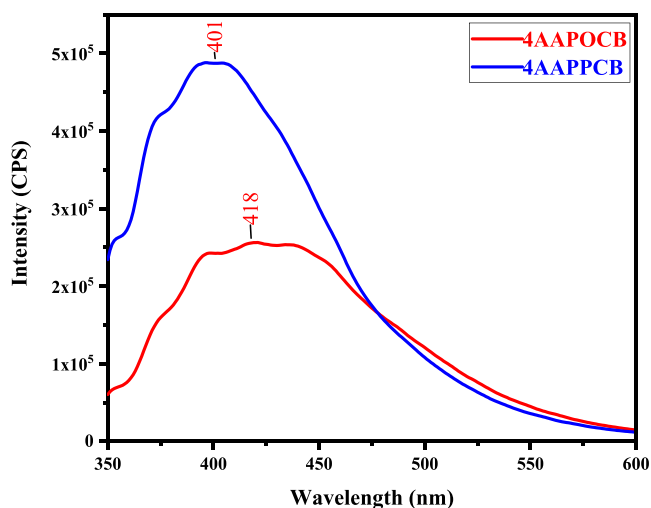


Figure 9. Photoluminescence spectrum of 4AAPOCB and 4AAPPCB.

4AAPPCB are presented in Figures 10 and 11. Furthermore, calculated FTIR spectra of the compounds are presented in Figure S5. Various absorption bands and their assignments are listed in Table 5.

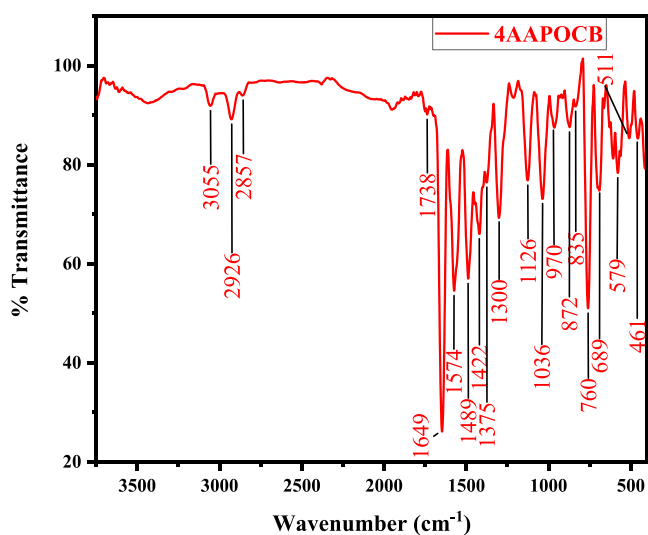


Figure 10. FTIR spectrum of 4AAPOCB.

3.6.1. Vibrations of the Azomethine Group. The C=N group exhibits a strong absorption band in the FTIR spectrum between 1690 and 1590 cm^{-1} .⁵¹ The stretching vibrations of the (CH=N) azomethine group, which are shreds of evidence of the formation of Schiff bases, are the cause of the sharp and strong bands that appear at 1649 and 1647 cm^{-1} for compounds I and II, respectively. The calculated values for C=N stretching appeared at 1640 and 1642 cm^{-1} , respectively. The yellow color of the product and the resulting -CH=N- bond both clearly indicate the formation of the Schiff base according to the X-ray diffraction results.

3.6.2. C-H and N-H Vibrations. The broad absorption band that usually appeared as a result of asymmetric stretching vibrations of the -NH₂ group in 4AAP in the range of 3200–3400 cm^{-1} disappeared because of the formation of azomethine linkage.⁵² For compounds I and II, the C-H stretching vibrations of the aromatic rings were observed at

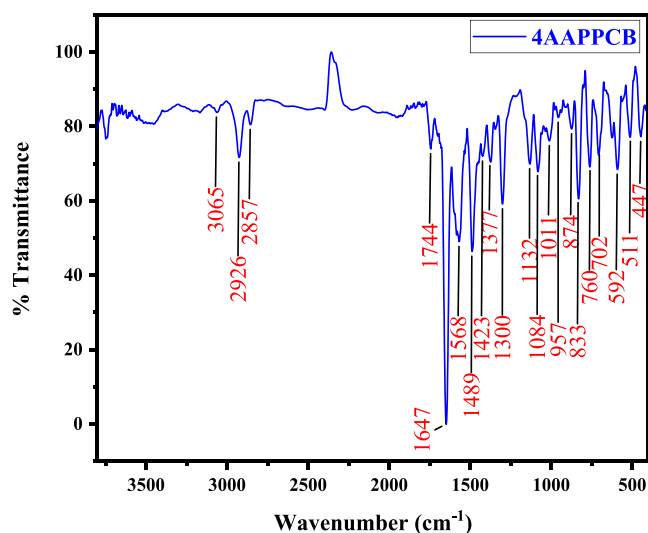


Figure 11. FTIR spectrum of 4AAPPCB.

Table 5. FTIR Vibrational Bands and Their Assignments for 4AAPOCB and 4AAPPCB

wave number (cm^{-1})					assignments
4AAPOCB		4AAPPCB			
experimental	calculated	experimental	calculated		
3055	3056	3065	3050	aromatic asymmetric C-H stretching vibration	
2926	2894	2926	2894	aliphatic asymmetric C-H stretching vibration	
2857		2857		aliphatic symmetric C-H stretching vibration	
1738	1718	1744	1718	C=O stretching vibrations of the carbonyl group	
1649	1640	1647	1680	CH=N stretching vibrations	
1574		1568		C=C aromatic skeletal vibrations	
1489	1466	1489	1466	N-CH ₃ symmetric deformation vibrations	
1422		1423		asymmetric in-plane bending vibration of -CH ₃	
1375		1377		symmetric in-plane bending vibration of -CH ₃	
1300	1280	1300	1280	C-N stretching vibration	
1126, 970	1106, 1120	1132, 1011, 957	1106	aromatic C-H in-plane bending vibration	
1036	1010	1084	1080	C-Cl stretching vibrations	
872, 835, 760	746	874, 833, 760	806, 760	aromatic C-H out-of-plane bending vibrations	
689		702		aromatic C-C in-plane bending	
579, 511	520, 590	592, 511		out-of-plane aromatic ring deformations (ring puckering)	
461		447	428	C-Cl deformation vibrations	

3055 and 3065 cm^{-1} , respectively. Sharp peaks in the range of 2800–3000 cm^{-1} in the spectra of both compounds supported the existence of the methyl group. The methyl group in compounds I at II shows C-H asymmetric and symmetric stretching vibrations at 2926 and 2857 cm^{-1} . In addition, its corresponding in-plane bending vibrations typically occurred

between 1370 and 1450 cm^{-1} .⁴⁹ Because of the asymmetric and symmetric in-plane bending vibrations of methyl groups, respectively, the spectra of compounds I and II exhibit sharp peaks at 1422, 1423, 1375, and 1377 cm^{-1} . Both compounds displayed symmetric N-CH₃ deformations at 1489 cm^{-1} . Simulated spectra for both the compounds exhibit absorption peaks at 3056 and 3050 cm^{-1} corresponding to aromatic C–H stretching vibration modes and the aliphatic C–H stretching vibrations of methyl groups appeared as a sharp peak at 2894 cm^{-1} for both the compounds.

In-plane bending modes of aromatic C–H are observed at the range of 950–1250 cm^{-1} .⁵³ The synthesized Schiff base compounds contain mono- and di-substituted benzene rings that give rise to different in-plane bending vibration peaks, and the peaks observed at 1126 and 970 cm^{-1} and at 1132, 1011, and 957 cm^{-1} for compounds I and II are due to aromatic in-plane bending vibrations of C–H bonds. Corresponding vibrational bands were observed at 1106 cm^{-1} in computed spectra. The out-of-bending modes of the C–H bond in phenyl rings appeared at 872, 835, and 760 cm^{-1} and at 874, 833, and 760 cm^{-1} for compounds I and II, respectively.⁵⁴ Bending modes of C–H bonds were observed as low-intensity sharp peaks in the range of 800 to 600 cm^{-1} in the computational spectrum.

3.6.3. C=O, C=C, and C–N Vibrations. The carbonyl group's stretching vibrations account for the medium-intensity peaks at 1738 and 1744 cm^{-1} , whereas the aromatic ring's skeletal vibrations account for the sharp peak at 1489 cm^{-1} for both compounds. Computed spectra also show a very strong C=O stretching peak at 1718 cm^{-1} . The C–N stretching vibrations of the heterocyclic ring account for the sharp peak at 1300 cm^{-1} and the same peak observed at 1280 cm^{-1} for both the compounds. Vibrations of aromatic ring deformation are typically observed below 700 cm^{-1} .⁵⁵ The C–C in-plane bending modes of the phenyl ring are assigned to the absorption peaks at 689 and 702 cm^{-1} , respectively, as are the corresponding out-of-plane bending ring puckering peaks at 579 and 511 cm^{-1} and at 592 and 511 cm^{-1} for compounds I and II.

3.6.4. C–Cl Vibrations. Ar–Cl stretching is usually observed in the range of 1100–1090 cm^{-1} for para-substituted derivatives and the same was observed in the range of 1060–1030 cm^{-1} for ortho-substituted compounds.⁵⁵ The fact that the C–Cl stretching vibration was observed at 1084 cm^{-1} for 4AAPPCB and 1036 cm^{-1} for 4AAPOCB indicates that the two compounds in question are ortho–para isomers. Furthermore, computed spectra also exhibit C–Cl stretching at 1080 and 1060 cm^{-1} . Between 370 and 500 cm^{-1} , aromatic C–Cl and ring deformations for chloro-substituted phenyl rings appeared. C–Cl deformations of compounds I and II account for the sharp peaks at 461 and 447 cm^{-1} , respectively.

3.7. Thermal Analysis. The thermal stability of organic crystals is crucial for a variety of practical NLO device applications. Crystals that can withstand high-intensity laser light and produce extremely precise results are thermally stable. The powdered samples of 4AAPOCB and 4AAPPCB were heated from room temperature to 700 °C at a rate of 20 °C/min in a nitrogen atmosphere for thermal analysis. The TG curve of the compounds is shown in Figure 12, which shows the weight loss of compounds I and II as a function of temperature. Both thermograms indicate that weight loss occurs in two stages. The fact that compounds 4AAPOCB and 4AAPPCB do not lose any weight below 200 °C indicates that

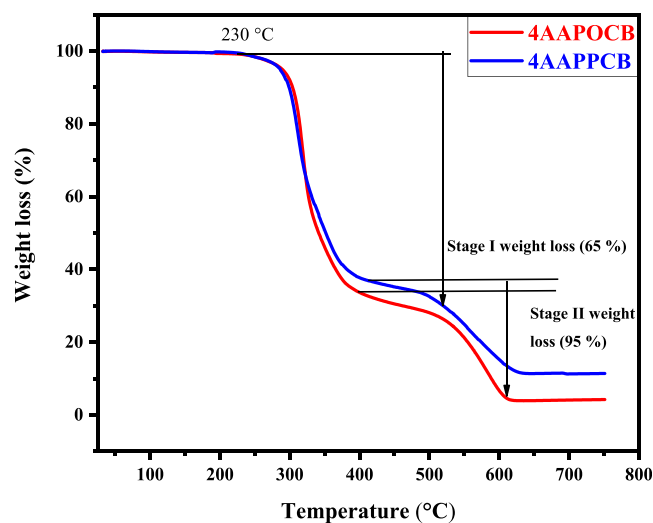


Figure 12. TG curves of 4AAPOCB and 4AAPPCB.

there are no physical impurities or water of crystallization present. The thermogram demonstrates a two-stage weight loss as the compound 4AAPPCB begins to decompose at 230 °C. The stage I weight loss of 62% was observed in the range of 230–400 °C; then, at the range of 400–638 °C, the second stage weight loss of 26% was observed after 638 °C, and 12% of the residue remained. The compound 4AAPOCB also starts to decompose after 230 °C, and there are two-stage weight losses observed. The stage I weight loss of 67% was observed in the range of 230–465 °C; then, at the range of 465 to 638 °C, the second-stage weight loss of 29% was observed. A residual mass of 4% remained at 638 °C.

The small exothermic event in DTA at 191 and 194 °C observed on both compounds may be due to phase transitions before the melting of the material. The second sharp endothermic event at 318 and 314 °C for 4AAPOCB and 4AAPPCB, respectively, affirms the melting followed by decomposition of the material. The obtained TG-DTA thermograms of the compounds are shown in Figures S1 and S2. The second broad endothermic DTA event at 559 °C for 4AAPPCB is due to the decomposition of the material, and at the end of the experiment, 12% of the residue remains at above 638 °C. In the case of 4AAPOCB, the broad exothermic DTA event at 583 °C indicates the decomposition.

The obtained DSC curves for 4AAPPCB show one endothermic event at 195 °C followed by two exothermic events at 316 and 556 °C. The obtained TG-DSC thermograms of the compounds are shown in Figures S3 and S4. The first endothermic event at 195 °C may be due to some phase change or recrystallization before melting, and the other two exothermic events are due to melting and decomposition of the sample. The sharp exothermic peak at 316 °C is due to the melting of the sample and is in good agreement with the DTA trace. The broad exothermic event near 558 °C appeared as a result of the complete decomposition of the materials. The DSC curve of 4AAPPCB also shows an endothermic event at 195.2 °C and successive exothermic events at 322.5 and 583.3 °C due to the melting and decomposition of the material, respectively. The DTA results coincide with the important weight loss shown by TG and are also in good agreement with DSC results. The sharp peak in DTA narrates the purity and appreciable crystallinity of the grown 4AAPPCB crystals. Thus,

the TG-DTA analysis concluded that both crystals can be used for NLO device applications up to a temperature of 190 °C.

3.8. Second-Order Nonlinear Property. The Kurtz–Perry powder method was used to investigate Schiff base compounds' SHG efficiency. The symmetry of the molecule directly affects the material's second-order nonlinearity. In general, a non-centrosymmetric structure is necessary for any material to become NLO active, and other factors like π -conjugation, impurities, crystalline defects, intermolecular interactions, and charge transfer have a significant impact. The powdered samples were taken in a capillary tube and exposed to a Q-switched Nd-Yag laser of a fundamental wavelength of 1064 nm. The energy of the laser pulse applied to the sample was 1.2 mJ per pulse with 10 ns and a pulse repetition rate of 10 Hz. The SHG signals of 81 and 26 mV were observed for compounds 4AAPOCB and 4AAPPCB, respectively, and the same experimental conditions used for standard references KDP and urea produced SHF signals of 23 and 70 mV, respectively. The comparative SHG efficiency of the compound I is 3.52 times greater than that of KDP and 1.15 times that of urea. Compound II has 1.13 times greater efficiency than KDP. The experimental and computational analysis showed the significant potential of compounds 4AAPOCB and 4AAPPCB as good contenders for NLO applications.

3.9. Computational Studies. **3.9.1. Optimized Molecular Geometries.** The molecular geometries of designed compounds 4AAPOCB and 4AAPPCB are shown in Figure 13.

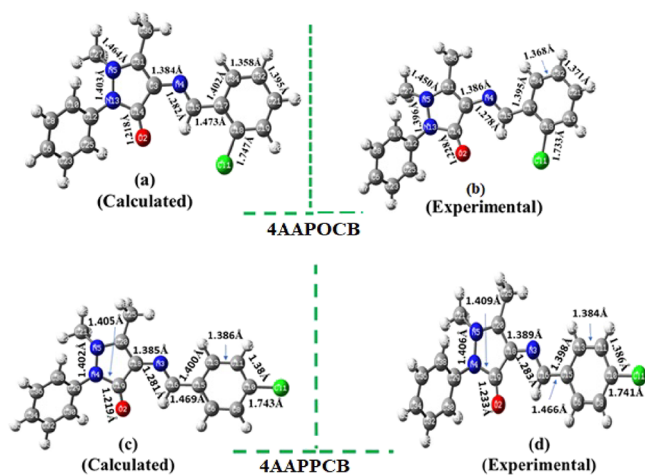


Figure 13. (a–d) Experimental and optimized geometric parameters of 4AAPOCB and 4AAPPCB.

The M06-2X functional and 6-31G* basis set is used to acquire the lowest energy structures. Figure 13a,b shows the calculated and experimental comparison of molecular geometries for the 4AAPOCB compound, whereas Figure 13c,d illustrates the compound 4AAPPCB. The calculated bond lengths for 4AAPOCB compound of Cl₁₁–C₁₈, C₁₅–N₄, and C₁₄–O₂ are found to be 1.747, 1.282, and 1.218 Å, which are near the experimental bond lengths of 1.733, 1.278, and 1.288 Å, respectively. In 4AAPPCB, the calculated bond lengths of Cl₁₁–C₁₀, C₁₆–N₃, and C₁₉–O₂ are 1.743, 1.281, and 1.219 Å, whereas experimental bond lengths are 1.741, 1.283, and 1.233 Å, respectively. The difference between the calculated and experimental values of both compounds is insignificant. The difference between the molecular geometries of 4AAPOCB

and 4AAPPCB compounds is that chlorine is present at the para position in 4AAPOCB, whereas in compound 4AAPPCB, chlorine is present at the ortho position, as a result of which it withdraws electrons through an inductive effect and releases electrons through resonance.

3.9.2. Linear Polarizability (α). The α values of compounds 4AAPOCB and 4AAPPCB were calculated at the M06-2X functional and 6-31G* basis set and are given in Table 6.

Table 6. Estimated Linear Polarizability Values (10^{-24} esu) of 4AAPOCB and 4AAPPCB at M06/6-311G* Levels of Theory

α comp.	4AAPOCB	4AAPPCB
α_{xx}	63.22	22.13
α_{xy}	5.25	1.86
α_{yy}	21.81	54.31
α_{xz}	−6.03	7.97
α_{yz}	−6.88	−12.51
α_{zz}	53.03	63.13
α_{iso}	46.02	46.52
α_{aniso}	41.60	45.47

Among all the tensors, α_{xx} values are relatively high, which suggest that polarization mostly occurs along the x axis. The 4AAPOCB and 4AAPPCB compounds showed isotropic values of 46.02×10^{-24} and 46.52×10^{-24} esu, respectively. Similarly, the 4AAPOCB and 4AAPPCB compounds showed anisotropic values of 41.60×10^{-24} and 45.47×10^{-24} esu, respectively. Compound 4AAPPCB showed relatively enhanced isotropic and anisotropic values as a result of the presence of chlorine atom at the para position.

3.9.3. Molecular Second-Order NLO Polarizability. The microscopic NLO characteristics of compounds are determined by calculating their second- and higher-order molecular nonlinear polarizability.⁵⁶ It is important to note down that molecular NLO polarizability and bulk-level NLO susceptibility are different parameters for judging NLO response properties. Molecular NLO polarizability (also called microscopic NLO polarizability) provides insights at molecular levels irrespective of bulk-level effects as determined by experiments. The calculated second-order molecular NLO polarizability (β) ($\times 10^{-30}$ esu) of 4AAPOCB and 4AAPPCB at the M06-2X/6-31G* method is collected in Table 7. Among all the tensors, β_{xxx} shows the highest values, which suggest that polarization occur along the x axis. The average β values of compounds

Table 7. The Estimated Second-Order NLO Polarizability (β_{ij} , 10^{-30} esu) of 4AAPOCB and 4AAPPCB at the M06-2X/6-31G* Levels of Theory

β	4AAPOCB	4AAPPCB
β_{xxx}	19.53	10.16
β_{xxy}	−0.13	−0.08
β_{xyy}	4.28	4.68
β_{yyy}	3.44	8.46
β_{xxz}	−13.24	1.20
β_{xyz}	−1.49	−0.37
β_{yyz}	0.94	0.60
β_{xzz}	−0.90	−0.23
β_{yzz}	0.31	−0.39
β_{zzz}	0.42	−3.76
$\beta_{//}$	14.74	8.106

4AAPOCB and 4AAPPCB are found to be 14.74×10^{-30} and 8.10×10^{-30} esu, respectively. To postulate a comprehensive visualization of the relationship between NLO properties and molecular axis, the second-order NLO polarizability unit spherical representation (USR)⁵⁷ of 4AAPOCB and 4AAPPCB was obtained at the M06-2X functional and 6-31G* levels of theory as presented in Figure 14.

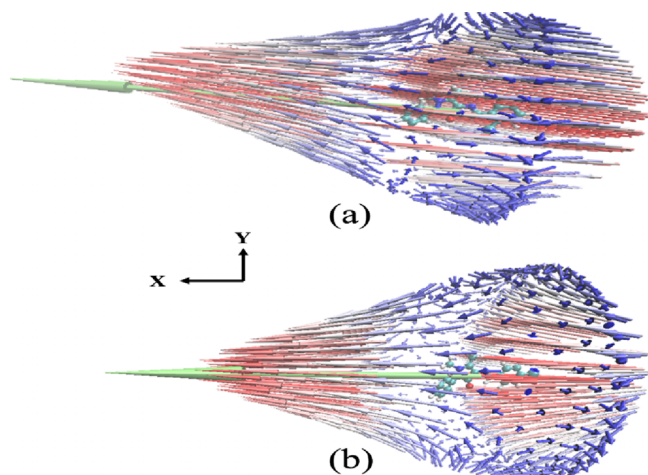


Figure 14. Unit sphere representation (red and blue arrows) of the first hyperpolarizability tensors for (a) 4AAPOCB and (b) 4AAPPCB. The green arrows represent the first hyperpolarizability vectors. Different scales have been employed in the representations of the effective dipoles and first hyperpolarizability vectors.

The blue and red arrows show the effective induced dipole moment, and the green arrow indicates the second-order NLO polarizability vectors. It is important to note that both USR representations show a nonsymmetric and one-directional induced dipole moment from chlorobenzyl toward pyrazole moieties. The second-order NLO polarizability vector is relatively larger for compound 4AAPOCB, and it is slightly tilted away from the x axis because of the ortho position of chlorine atoms in compound 4AAPOCB (see Figure 13).

3.9.4. TD-DFT Calculations. TD-DFT computations of 4AAPOCB and 4AAPPCB were performed at the TD-M06-2X functional and 6-31G* basis set to ascertain the source of second-order NLO polarizability. It is conventional to utilize a well-known two-level approximation to pinpoint the origin of β amplitudes at least for one dominant longitudinal component as given by eq 7.⁵⁸

$$\beta_L = \left(\frac{3}{2}\right) \Delta\mu \frac{f_0}{\Delta E^3} \quad (7)$$

where β_L is the longitudinal component, and it is β_{xxx} here. $\Delta\mu$ is the change in dipole moment between the ground and excited state, ΔE is the transition energy, and f_0 is the oscillator strength from the ground state to the excited state. From eq 7, it can be observed that β_L is directly related to $\Delta\mu$ and f_0 but inversely related to the cube of ΔE , which may be considered as a crucial factor. The transition energies (ΔE 's), oscillator strength (f_0), and percentage configuration interaction (% C.I.) for electronic excitations of compounds 4AAPOCB and 4AAPPCB are collected in Table 8. In $S_0 \rightarrow S_1$ electronic excitation, compound 4AAPPCB showed a lower transition energy value as compared to compound 4AAPOCB, which might lead to better amplitude in compound 4AAPOCB.

Table 8. The Oscillator Strength (f_0), Transition Energies (ΔE 's), and Configuration Interaction (C.I.) of Compounds 4AAPOCB and 4AAPPCB at the M06-2X Functional and 6-31G* Basis Set

compounds	electronic excitation	ΔE (eV)	f_0	transitions	% C.I.
4AAPOCB	$S_0 \rightarrow S_1$	4.121	0.983	H \rightarrow L	67
4AAPPCB	$S_0 \rightarrow S_1$	4.148	1.197	H \rightarrow L	69

3.9.5. Frontier Molecular Orbitals (FMOs). Frontier molecular orbitals provide a great idea to understand the type of intramolecular charge transfer (ICT) process, stability of compounds, and origin of electronic transition.⁵⁹ The HOMO and LUMO distribution patterns of compounds 4AAPOCB and 4AAPPCB are computed at the M06-2X functional and 6-31G* basis set as shown in Figure 15. It can

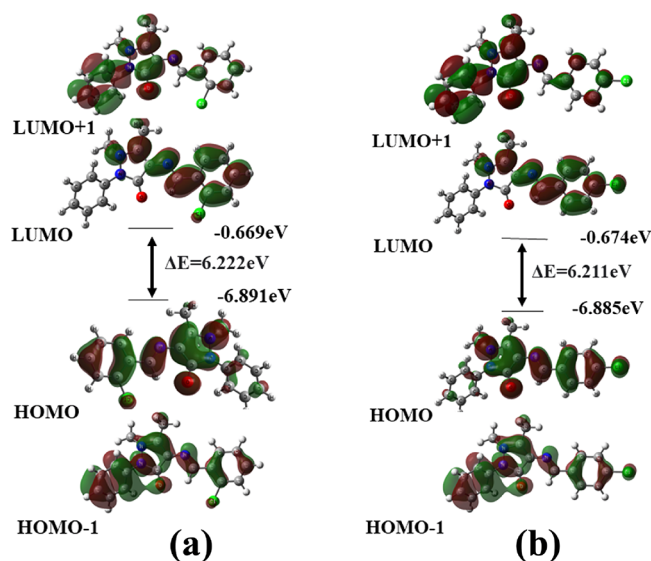


Figure 15. The highest occupied molecular orbitals (HOMOs) and lowest unoccupied molecular orbitals (LUMOs) for compounds 4AAPOCB (a) and 4AAPPCB (b). The iso-value is ± 0.001 a. u.

be observed from Figure 15 that both compounds show similar HOMO and LUMO formation. In HOMO formation of compounds 4AAPOCB and 4AAPPCB, the delocalization of wavefunction occurs over the whole molecule, whereas in the case of LUMO, charge delocalization occurs except for O and N atoms and the benzene ring that are not involved in the formation of LUMO. The transition from HOMO to LUMO mainly demonstrates the redistribution of charge density. The calculated energy values of HOMO for both compounds 4AAPOCB and 4AAPPCB are -6.885 and -6.891 eV, respectively, whereas their LUMO orbitals show energy values of -0.674 and -0.669 eV, respectively. The orbital energy gap (ΔE_{H-L}) that is calculated for HOMO–LUMO of both compounds 4AAPOCB and 4AAPPCB is 6.211 and 6.22 eV, respectively. There is a minor energy gap of 0.01 eV between compounds 4AAPOCB and 4AAPPCB because of structural similarity.

3.9.6. Molecular Electrostatic Potentials (MEPs). The molecular electrostatic potential (MEP) is an interpretative tool for the determination of intramolecular interactions and electron density distribution over the molecule. It describes the location for incoming electrophile and nucleophile attacks by

measuring the strength of the nearby charges, nuclei, and electrons at specific positions. Electrostatic potential values are represented by different color codes, and the order of potential increment is red < orange < yellow < green < light blue < blue. The maximum positive electrostatic potential is indicated by the blue color, and the red color is considered the maximum negative electrostatic potential.^{60,61} The green color is the neutral region because it is close to zero potential. The MEP diagrams of compounds 4AAPOCB and 4AAPPCB obtained at the M06-2X functional and 6-31G* basis set are shown in Figure 16. The red color represents the maximum negative

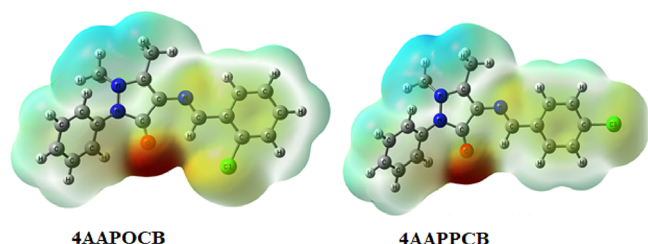


Figure 16. Molecular electrostatic potential surface analysis of compounds 4AAPOCB and 4AAPPCB at the M06-2X functional and 6-31G* basis set. The iso-value is ± 0.001 a. u.

electrostatic potential for the oxygen atom as a terminal group in both compounds, and it is a highly favorable region for the electrophilic attack. The indication of blue color in methyl groups and hydrogen atoms reveals that there is a greater positive potential that will be the attacking side for the nucleophile. Moreover, chlorine with a slight yellow color represents intermediate electrostatic potentials in both 4AAPOCB and 4AAPPCB molecules. It can be seen that both the compounds have significant charge separation in the form of highly negative and positive potentials.

4. CONCLUSIONS

The new NLO active Schiff base compounds 4AAPOCB and 4AAPPCB were synthesized through the condensation reaction of 4-aminoantipyrine with 2-chlorobenzaldehyde and 4-chlorobenzaldehyde, respectively. Single crystals of the synthesized compounds were grown in methanol at room temperature by the slow solvent evaporation method. The SCXRD analysis was used to identify the crystal structure and lattice parameters; the isomeric compounds crystallized into an orthorhombic system with space groups $P2_12_12_1$ and $Pbca$, respectively. Moreover, the sharp peak in PXRD patterns appears to have good crystallinity. Elemental analysis results reveal stoichiometry, and there is good agreement with calculated values. Vibration analysis (FTIR) and electronic spectral analysis (UV–vis) have been performed, and the results have been compared to the corresponding computed spectra and found to be in good agreement. The UV–vis–NIR transmittance spectrum of the crystals exhibits wide optical transparency (85%) in visible and near-infrared regions, and their photoluminescence emission spectrum shows broad violet emission bands. Because 4AAPOCB has a powder SHG efficiency that is 3.52 times greater than that of KDP and 1.15 times that of urea, it can be used to fabricate optical devices. Quantum chemical methods were used to optimize the molecular geometries of synthesized molecules. The linear optical and second-order NLO properties at the molecular level were calculated for compounds 4AAPOCB and

4AAPPCB obtained at the M06-2X functional and 6-31G* basis set. The 4AAPOCB and 4AAPPCB compounds showed isotropic values of 46.02×10^{-24} and 46.52×10^{-24} esu, respectively. Similarly, the 4AAPOCB and 4AAPPCB compounds showed anisotropic values of 41.60×10^{-24} and 45.47×10^{-24} esu, respectively. The compound 4AAPPCB showed relatively enhanced isotropic and anisotropic values due to the presence of chlorine atom at the para position. Besides this, the average β values of compounds 4AAPOCB and 4AAPPCB are found to be 14.74×10^{-30} and 8.10×10^{-30} esu, respectively, which indicated a decent potential of synthesized compounds for NLO applications.

■ ASSOCIATED CONTENT

Supporting Information

The Supporting Information is available free of charge at <https://pubs.acs.org/doi/10.1021/acsomega.2c08305>.

The calculated value of the dipole moment (μ , debye), linear polarizability (α , 10^{-24} esu), and second-order NLO polarizability (β , 10^{-30} esu) with different functionals and 6-311G* basis set; the bond lengths (\AA) and bond angles ($^\circ$) along with their differences among calculated and experimental values and root mean square (RMSE) values; TG-DTA and TG-DSC thermogram of compounds I and II; and the computed and experimental IR spectra of the compounds (PDF)

■ AUTHOR INFORMATION

Corresponding Authors

Saravanabhavan Munusamy – Department of Chemistry, KPR Institute of Engineering and Technology, Coimbatore 641407 Tamil Nadu, India; orcid.org/0000-0003-2698-0804; Email: drmsbavan@gmail.com

Marimuthu Sekar – Department of Chemistry, Sri Ramakrishna Mission Vidyalyaya College of Arts and Science, Coimbatore 641 020 Tamil Nadu, India; Email: msekar966@gmail.com

Authors

Amsaveni Arumugam – Department of Chemistry, Sri Ramakrishna Mission Vidyalyaya College of Arts and Science, Coimbatore 641 020 Tamil Nadu, India

Ramesh Shanmugam – Department of Chemistry, Sri Ramakrishna Mission Vidyalyaya College of Arts and Science, Coimbatore 641 020 Tamil Nadu, India; Department of Chemistry, Adithya Institute of Technology, Coimbatore 641 107 Tamil Nadu, India; orcid.org/0000-0002-0506-0294

Shabbir Muhammad – Department of Chemistry, College of Science, King Khalid University, Abha 61413, Saudi Arabia; orcid.org/0000-0003-4908-3313

Hamed Algarni – Department of Physics, College of Science, King Khalid University, Abha 61413, Saudi Arabia

Complete contact information is available at: <https://pubs.acs.org/doi/10.1021/acsomega.2c08305>

Funding

The authors extend their appreciation to the Deanship of Scientific Research at King Khalid University for funding the work through Group Research Project under grant number RGP2/272/44.

Notes

The authors declare no competing financial interest. CCDC 2248220 and 2225635 contain the supplementary crystallographic data for this paper. These data can be obtained free of charge via <http://www.ccdc.cam.ac.uk/conts/retrieving.html> (or from the Cambridge Crystallographic Data Centre, 12, Union Road, Cambridge CB21EZ, UK; fax: +44 1223 336033) or e-mail: deposit@ccdc.cam.ac.uk.

ACKNOWLEDGMENTS

The authors acknowledge STIC Kochi, India, for single-crystal X-ray diffraction and TG-DTA analysis; Karunya Deemed University, Coimbatore, India, for UV–Visible-NIR, photoluminescence, and FTIR spectral analysis.

REFERENCES

- (1) Munn, R. W.; Ironside, C. N. *Principles and Applications of Nonlinear Optical Materials*; Springer, 1993, DOI: 10.1007/978-94-011-2158-3.
- (2) Bloembergen, N. Nonlinear Optics: Past, Present, and Future. *IEEE J. Sel. Top. Quantum Electron.* **2000**, *6*, 876–880.
- (3) Bosshard, C.; Sutter, K.; Prêtre, P.; Hulliger, J.; Flörsheimer, M.; Kaatz, P.; Günter, P. *Organic Nonlinear Optical Materials*; CRC press, 2020, DOI: 10.4324/9780429114090.
- (4) Nalwa, H. S.; Miyata, S. *Nonlinear Optics of Organic Molecules and Polymers*; CRC press, 1996.
- (5) Derkowska-Zielinska, B.; Barwiolek, M.; Cassagne, C.; Boudebs, G. Nonlinear Optical Study of Schiff Bases Using Z-Scan Technique. *Opt. Laser Technol.* **2020**, *124*, 105968.
- (6) Sathya Priyadarshini, G.; Edathil, V.; Selvi, G. Non Linear Optical Properties of Potent Quinoline Based Schiff Bases. *Mater. Today Proc.* **2022**, *51*, 1746–1750.
- (7) Bhat, K.; Chang, K. J.; Aggarwal, M. D.; Wang, W. S.; Penn, B. G.; Frazier, D. O. Synthesis and Characterization of Various Schiff Bases for Non-Linear Optical Applications. *Mater. Chem. Phys.* **1996**, *44*, 261–266.
- (8) Qin, W.; Long, S.; Panunzio, M.; Biondi, S. Schiff Bases: A Short Survey on an Evergreen Chemistry Tool. *Molecules* **2013**, *18*, 12264–12289.
- (9) Abu-Dief, A. M.; Mohamed, I. M. A. A Review on Versatile Applications of Transition Metal Complexes Incorporating Schiff Bases. *Beni-Suef Univ. J. Basic Appl. Sci.* **2015**, *4*, 119–133.
- (10) Gomha, S. M.; Ahmed, H. A.; Shaban, M.; Abolibda, T. Z.; Khushaim, M. S.; Alharbi, K. A. Synthesis, Optical Characterizations and Solar Energy Applications of New Schiff Base Materials. *Materials* **2021**, *14*, 3718.
- (11) Berhanu, A. L.; Gaurav, Mohiuddin, I.; Malik, A. K.; Aulakh, J. S.; Kumar, V.; Kim, K. H. A Review of the Applications of Schiff Bases as Optical Chemical Sensors. *TrAC - Trends Anal. Chem.* **2019**, *116*, 74–91.
- (12) Udhayakumari, D.; Inbaraj, V. A Review on Schiff Base Fluorescent Chemosensors for Cell Imaging Applications. *J. Fluoresc.* **2020**, *30*, 1203–1223.
- (13) Li, X. L.; Xie, B.; Feng, J. S.; Lai, C.; Bai, X. X.; Li, T.; Zhang, D. L.; Mou, W. Y.; Wen, L.; Gu, Y. T. 2-Pyridinecarboxaldehyde-Based Schiff Base as an Effective Corrosion Inhibitor for Mild Steel in HCl Medium: Experimental and Computational Studies. *J. Mol. Liq.* **2022**, *345*, 117032.
- (14) Fang, W.; Cao, Z.; Liu, Q.; Chu, Y.; Zhu, H.; Zhou, W.; Yang, J. A Novel Star-Shaped Schiff Base Compound: Synthesis, Properties and Application in w-LEDs. *Results Opt.* **2022**, *7*, 100228.
- (15) Zhang, J.; Xu, L.; Wong, W.-Y. Energy Materials Based on Metal Schiff Base Complexes. *Coord. Chem. Rev.* **2018**, *355*, 180–198.
- (16) Segura, J. L.; Mancheño, M. J.; Zamora, F. Covalent Organic Frameworks Based on Schiff-Base Chemistry: Synthesis, Properties and Potential Applications. *Chem. Soc. Rev.* **2016**, *45*, 5635–5671.
- (17) Kaur, M.; Kumar, S.; Yusuf, M.; Lee, J.; Brown, R. J. C.; Kim, K.-H.; Malik, A. K. Post-Synthetic Modification of Luminescent Metal-Organic Frameworks Using Schiff Base Complexes for Biological and Chemical Sensing. *Coord. Chem. Rev.* **2021**, *449*, 214214.
- (18) Adeel, M.; Khalid, M.; Ullah, M. A.; Muhammad, S.; Khan, M. U.; Tahir, M. N.; Khan, I.; Asghar, M.; Mughal, K. S. Exploration of CH–F & CH–H Mediated Supramolecular Arrangements into Fluorinated Terphenyls and Theoretical Prediction of Their Third-Order Nonlinear Optical Response. *RSC Adv.* **2021**, *11*, 7766–7778.
- (19) Shehzad, R. A.; Muhammad, S.; Iqbal, J.; Al-Sehemi, A. G.; Yaseen, M.; Aloui, Z.; Khalid, M. Exploring the Optoelectronic and Third-Order Nonlinear Optical Susceptibility of Cross-Shaped Molecules: Insights from Molecule to Material Level. *J. Mol. Model.* **2021**, *27*, 12.
- (20) Khalid, M.; Ali, A.; De la Torre, A. F.; Marrugo, K. P.; Concepcion, O.; Kamal, G. M.; Muhammad, S.; Al-Sehemi, A. G. Facile Synthesis, Spectral (IR, Mass, UV–Vis, NMR), Linear and Nonlinear Investigation of the Novel Phosphonate Compounds: A Combined Experimental and Simulation Study. *ChemistrySelect* **2020**, *5*, 2994–3006.
- (21) Rafiq, M.; Khalid, M.; Tahir, M. N.; Ahmad, M. U.; Khan, M. U.; Naseer, M. M.; Braga, A. A. C.; Muhammad, S.; Shafiq, Z. Synthesis, XRD, Spectral (IR, UV–Vis, NMR) Characterization and Quantum Chemical Exploration of Benzoimidazole-Based Hydrazones: A Synergistic Experimental-Computational Analysis. *Appl. Organomet. Chem.* **2019**, *33*, 1–17.
- (22) Khan, B.; Khalid, M.; Shah, M. R.; Tahir, M. N.; Khan, M. U.; Ali, A.; Muhammad, S. Efficient Synthesis by Mono-Carboxy Methylation of 4,4'-Biphenol, X-Ray Diffraction, Spectroscopic Characterization and Computational Study of the Crystal Packing of Ethyl 2-((4'-Hydroxy-[1,1'-Biphenyl]-4-Yl)Oxy)Acetate. *ChemistrySelect* **2019**, *4*, 9274–9284.
- (23) Muhammad, S.; Hussain, S.; Chen, X.; Al-Sehemi, A. G.; Li, Z. J.; Lai, C. H.; Iqbal, J. A Dual Approach to Study the Synthesis, Crystal Structure and Nonlinear Optical Properties of Binuclear Pd(II) Complex of 3-Methyl-5-(Trifluoromethyl) Pyrazole and Its Potential Quantum Chemical Analogues. *Inorg. Chim. Acta* **2019**, *494*, 160–167.
- (24) Kumar, S.; Muhammad, S.; Koh, J.; Khalid, M.; Ayub, K. A Combined Experimental and Computational Study of 2,2'-(Diazene-1,2-Diylbis(4,1-Phenylene))Bis(6-(Butylamino)-1H-Benzo[de]-Isoquinoline-1,3(2H)-Dione): Synthesis, Optical and Nonlinear Optical Properties. *Optik* **2019**, *192*, 162952.
- (25) Marinescu, M.; Cinteza, L.-O.; Popa, C.-V.; Gifu, I. C.; Burlacu, S. G.; Petcu, C. Synthesis, Characterization and Antimicrobial Activities of Some Schiff Bases with Non-Linear Optical Applications. **2022**, *40*, DOI: 10.3390/chemproc2022007040.
- (26) Günter, P. *Nonlinear Optical Effects and Materials*; Springer, 2012; Vol. 72.
- (27) Zyss, J. *Molecular Nonlinear Optics: Materials, Physics, and Devices*; Academic press, 2013.
- (28) Hussain, A.; Khan, M. U.; Ibrahim, M.; Khalid, M.; Ali, A.; Hussain, S.; Saleem, M.; Ahmad, N.; Muhammad, S.; Al-Sehemi, A. G.; Sultan, A. Structural Parameters, Electronic, Linear and Nonlinear Optical Exploration of Thiopyrimidine Derivatives: A Comparison between DFT/TDDFT and Experimental Study. *J. Mol. Struct.* **2020**, *1201*, 127183. DOI: 10.1016/j.molstruc.2019.127183.
- (29) Khan, M. U.; Iqbal, J.; Khalid, M.; Hussain, R.; Braga, A. A. C.; Hussain, M.; Muhammad, S. Designing Triazatruxene-Based Donor Materials with Promising Photovoltaic Parameters for Organic Solar Cells. *RSC Adv.* **2019**, *9*, 26402–26418.
- (30) Adeel, M.; Khalid, M.; Ullah, M. A.; Muhammad, S.; Khan, M. U.; Tahir, M. N.; Khan, I.; Asghar, M.; Mughal, K. S. Exploration of CH–F & CF–H Mediated Supramolecular Arrangements into Fluorinated Terphenyls and Theoretical Prediction of Their Third-Order Nonlinear Optical Response. *RSC Adv.* **2021**, *11*, 7766–7778.
- (31) Haroon, M.; Khalid, M.; Akhtar, T.; Tahir, M. N.; Khan, M. U.; Muhammad, S.; Al-Sehemi, A. G.; Hameed, S. Synthesis, Crystal

Structure, Spectroscopic, Electronic and Nonlinear Optical Properties of Potent Thiazole Based Derivatives: Joint Experimental and Computational Insight. *J. Mol. Struct.* **2020**, *1202*, 127354. DOI: 10.1016/j.molstruc.2019.127354.

(32) Sakthivel, A.; Jeyasubramanian, K.; Thangagiri, B.; Raja, J. D. Recent Advances in Schiff Base Metal Complexes Derived from 4-Aminoantipyrine Derivatives and Their Potential Applications. *J. Mol. Struct.* **2020**, *1222*, 128885.

(33) Murtaza, S.; Akhtar, M. S.; Kanwal, F.; Abbas, A.; Ashiq, S.; Shamim, S. Synthesis and Biological Evaluation of Schiff Bases of 4-Aminophenazone as an Anti-Inflammatory, Analgesic and Antipyretic Agent. *J. Saudi Chem. Soc.* **2017**, *21*, S359–S372.

(34) Chitra Devi, A.; Siva, V.; Thangarasu, S.; Athimoolam, S.; Asath Bahadur, S. Supramolecular Architecture, Thermal, Quantum Chemical Analysis and in Vitro Biological Properties on Sulfate Salt of 4-Aminoantipyrine. *J. Mol. Struct.* **2021**, *1245*, 131033.

(35) Khalid, M.; Ali, A.; Rehman, M. F. U.; Mustaqeem, M.; Ali, S.; Khan, M. U.; Asim, S.; Ahmad, N.; Saleem, M. Exploration of Noncovalent Interactions, Chemical Reactivity, and Nonlinear Optical Properties of Piperidone Derivatives: A Concise Theoretical Approach. *ACS Omega* **2020**, *5*, 13236–13249.

(36) Khalid, M.; Shafiq, I.; Umm-e-Hani; Mahmood, K.; Hussain, R.; ur Rehman, M. F.; Assiri, M. A.; Imran, M.; Akram, M. S. Effect of Different End-Capped Donor Moieties on Non-Fullerenes Based Non-Covalently Fused-Ring Derivatives for Achieving High-Performance NLO Properties. *Sci. Rep.* **2023**, *13*, 1–16.

(37) Khan, I.; Khalid, M.; Adeel, M.; Niaz, S. I.; Shafiq, I.; Muhammad, S.; Braga, A. A. C. Palladium-Catalyzed Synthesis of 5-(Arylated) Pyrimidines, Their Characterization, Electronic Communication, and Non-Linear Optical Evaluations. *J. Mol. Struct.* **2021**, *1237*, 130408.

(38) Khalid, M.; Arshad, M. N.; Murtaza, S.; Shafiq, I.; Haroon, M.; Asiri, A. M.; Figueirêdo de AlcântaraMorais, S.; Braga, A. A. C. Enriching NLO Efficacy via Designing Non-Fullerene Molecules with the Modification of Acceptor Moieties into ICIF2F: An Emerging Theoretical Approach. *RSC Adv.* **2022**, *12*, 13412–13427.

(39) Khan, M. U.; Khalid, M.; Shafiq, I.; Khera, R. A.; Shafiq, Z.; Jawaria, R.; Shafiq, M.; Alam, M. M.; Braga, A. A. C.; Imran, M.; Kanwal, F.; Xu, Z.; Lu, C. Theoretical Investigation of Nonlinear Optical Behavior for Rod and T-Shaped Phenothiazine Based D- π -A Organic Compounds and Their Derivatives. *J. Saudi Chem. Soc.* **2021**, *25*, 101339.

(40) Ramesh, K. S.; Saravanabhavan, M.; Rajkumar, M.; Edison, D.; Sekar, M.; Muhammad, S.; Al-Sehemi, A. G. Synthesis, Growth, Structural, Thermal, Third Order Nonlinear and Computational Studies of Organic Single Crystal: 2-Amino-4-Picolinium 2-Chloro-4-Nitrobenzoate. *Opt. Mater.* **2019**, *96*, 109341.

(41) Zaitseva, N. P.; Rashkovich, L. N.; Bogatyreva, S. V. Stability of KH₂PO₄ and K(H,D)2PO₄ Solutions at Fast Crystal Growth Rates. *J. Cryst. Growth* **1995**, *148*, 276–282.

(42) Sheldrick, G. M. A Short History of SHELX. *Acta Crystallogr. Sect. A Found. Crystallogr.* **2008**, *64*, 112–122.

(43) Sheldrick, G. M. Crystal Structure Refinement with SHELXL. *Acta Crystallogr. Sect. C Struct. Chem.* **2015**, *71*, 3–8.

(44) Frisch, M. J.; Trucks, G. W.; Schlegel, H. B.; Scuseria, G. E.; Robb, M. A.; Cheeseman, J. R.; Scalmani, G.; Barone, V.; Petersson, G. A.; Nakatsuji, H. *Gaussian 16 Revision a. 03.* 2016; Gaussian Inc.: Wallingford CT 2016, 2 (4).

(45) Muhammad, S.; Shehzad, R. A.; Iqbal, J.; Al-Sehemi, A. G.; Saravanabhavan, M.; Khalid, M. Benchmark Study of the Linear and Nonlinear Optical Polarizabilities in Proto-Type NLO Molecule of Para -Nitroaniline. *J. Theor. Comput. Chem.* **2019**, *18* (). DOI: 10.1142/S0219633619500305.

(46) Lai, C.-H.; Muhammad, S.; Al-Sehemi, A. G.; Chaudhry, A. R. A Systematic Study of the Effects of Thionation in Naphthalene Dimide Derivatives to Tune Their Nonlinear Optical Properties. *J. Mol. Graphics Modell.* **2019**, *87*, 68–75.

(47) Saeed, A.; Muhammad, S.; Rehman, S.; Bibi, S.; Al-Sehemi, A. G.; Khalid, M. Exploring the Impact of Central Core Modifications

among Several Push-Pull Configurations to Enhance Nonlinear Optical Response. *J. Mol. Graphics Modell.* **2020**, *100*, 107665.

(48) Muhammad, S. Quantum Chemical Design of Triple Hybrid Organic, Inorganic and Organometallic Materials: An Efficient Two-Dimensional Second-Order Nonlinear Optical Material. *Mater. Chem. Phys.* **2018**, *220*, 286–292.

(49) Mohan, J. *Organic Spectroscopy: Principles and Applications*; Narosa Publishing House: India, 2000.

(50) Issa, R. M.; Khedr, A. M.; Rizk, H. F. UV-Vis, IR and ¹H NMR Spectroscopic Studies of Some Schiff Bases Derivatives of 4-Aminoantipyrine. *Spectrochim. Acta - Part A Mol. Biomol. Spectrosc.* **2005**, *62*, 621–629.

(51) Bartyzel, A. Synthesis, Thermal Study and Some Properties of N₂O₄—Donor Schiff Base and Its Mn(III), Co(II), Ni(II), Cu(II) and Zn(II) Complexes. *J. Therm. Anal. Calorim.* **2017**, *127*, 2133–2147.

(52) El-Ghamaz, N. A.; Ghoneim, M. M.; El-Sonbati, A. Z.; Diab, M. A.; El-Bindary, A. A.; Abd El-Kader, M. K. Synthesis and Optical Properties Studies of Antipyrine Derivatives Thin Films. *J. Saudi Chem. Soc.* **2017**, *21*, S339–S348.

(53) Varsányi, G. *Vibrational Spectra of Benzene Derivatives*; Elsevier, 2012.

(54) Smith, B. *Infrared Spectral Interpretation: A Systematic Approach*; CRC Press: London, 1998.

(55) Socrates, G. *Infrared Characteristic Group Frequencies. Tables and Charts*; Wiley, 2001. DOI: 10.1016/0003-2670(94)80274-2.

(56) Muhammad, S. Connecting Two Intrinsic Electron Donor and Acceptor Moieties through Distinctive π -Bridging Units to Explore Their Optical and Nonlinear Optical Properties. *Mater. Sci. Semicond. Process.* **2022**, *152*, 107064.

(57) Ye, J.-T.; Liu, J.-H.; Zhang, Q.; Qiu, Y.-Q.; Wang, L.-H. Tuning of Second-Order Nonlinear Optical Properties Based on [2.2]-Paracyclophanes Isomer: The Relative Configuration and Polarizable Environment. *J. Phys. Chem. C* **2020**, *124*, 21692–21701.

(58) Muhammad, S.; Xu, H.; Su, Z.; Fukuda, K.; Kishi, R.; Shigeta, Y.; Nakano, M. A New Type of Organic–Inorganic Hybrid NLO-Phore with Large off-Diagonal First Hyperpolarizability Tensors: A Two-Dimensional Approach. *Dalton Trans.* **2013**, *42*, 15053–15062.

(59) Saba, A.; Sarwar, F.; Muhammad, S.; Ilyas, M.; Iqbal, J.; Al-Sehemi, A. G.; Ayub, K.; Amjad Gilani, M.; Adnan, M. Insighting the Inhibitory Potential of Novel Modafinil Drug Derivatives against Estrogen Alpha (ER α) of Breast Cancer through a Triple Hybrid Computational Methodology. *J. Mol. Liq.* **2022**, *366*, 120234.

(60) Sarwar, F.; Muhammad, S.; Shafiq-ur-Rehman; Bibi, S.; Al-Sehemi, A. G.; Algarni, H.; Kumar, S. Insighting the Systematic Impact of Shape, Size and Substitution of Heteroatoms in Quinoidal Oligomers to Tune Their Optoelectronic Properties. *Opt. Quantum Electron.* **2022**, *54*, 356.

(61) Muhammad, S. Symmetric vs. Asymmetric: Which One Is the Better Molecular Configuration for Achieving Robust NLO Response? *J. Mol. Graphics Modell.* **2022**, *114*, 108209.